A&A 506, 1437–1443 (2009)
DOI: 10.1051/0004-6361/200912616

Astronomy & Astrophysics

Electron beam – plasma system with the return current and directivity of its X-ray emission

M. Karlický and J. Kašparová

Astronomical Institute of the Academy of Sciences of the Czech Republic, 25165 Ondřejov, Czech Republic
e-mail: [karlicky;kasparov]@asu.cas.cz

Received 2 June 2009 / Accepted 29 July 2009

ABSTRACT

Aims. An evolution of the electron distribution function in the beam-plasma system with the return current is computed numerically for different parameters. The X-ray bremsstrahlung corresponding to such an electron distribution is calculated and the directivity of the X-ray emission is studied.
Methods. For computations of the electron distribution functions we used a 3-D particle-in-cell electromagnetic code. The directivity of the X-ray emission was calculated using the angle-dependent electron-ion bremsstrahlung cross-section.
Results. It was found that the resulting electron distribution function depends on the magnetic field assumed along the electron beam propagation direction. For small magnetic fields the electron distribution function becomes broad in the direction perpendicular to the beam propagation due to the Weibel instability and the return current is formed by the electrons in a broad and shifted bulk of the distribution. On the other hand, for stronger magnetic fields the distribution is more extended in the beam-propagation direction and the return current is formed by the electrons in the extended distribution tail. In all cases, the anisotropy of the electron distribution decreases rapidly due to fast collisionless processes. However, the magnetic field reduces this anisotropy decrease. The X-ray directivity shows the same trend and it is always closer to the isotropic case than that in a simple beaming model.

Key words. Sun: flares – Sun: particle emission – Sun: X-rays, gamma rays

1. Introduction

It is commonly believed that the hard X-ray emission in solar flares is produced by the bremsstrahlung process of energetic electrons in dense layers of the solar atmosphere (Brown 1971; Tandberg-Hanssen & Emslie 1988).

It is also known that up to now this scenario has several unresolved drawbacks as summarized in the paper by Brown et al. (1990). For example, the bremsstrahlung mechanism generating the hard X-ray bursts is of a very low efficiency and therefore huge electron beam fluxes $E_F = 10^9$–10^{12} erg s^{-1} cm^{-2} are required for an explanation of the observed X-ray fluxes (Hoyng et al. 1978). It means that at the acceleration site in the low corona with a relatively low density ($n_e \sim 10^9$ cm^{-3}), a substantial part of all plasma electrons needs to be accelerated. Furthermore, these electron beams represent huge electric currents that have to be neutralized by the return currents. The return current is a natural part of any beam-plasma system (van den Oord 1990).

The beam-plasma interaction has been studied for a long time, starting with the paper by Bohm & Gross (1949). While the first 1-D models considered the electrostatic aspects of this interaction (two-stream instability, generation of Langmuir waves, and quasi-linear relaxation of the beam, see e.g. Melrose 1980; Birdsall & Langdon 1985; Benz 1993; Karlický 1997, and the references therein), new 3-D studies include the return current and electromagnetic effects which lead to many further instabilities (Weibel, filamentation, oblique, Bell, Buneman, and so on, see Karlický 2009; Karlický & Bárta 2009; Bret 2009). (Remark: The Weibel instability in the sense used here and in the paper by Nishikawa et al. (2008) is also known as the filamentation instability (Bret 2009).) To cover all these processes, especially inductive processes neutralizing the total electric current, in the present study we use a general and fully self-consistent (basic plasma physics) approach – a 3-D electromagnetic particle-in-cell (PIC) modelling.

All the abovementioned processes necessarily modify the electron distribution function in the flare X-ray source. Moreover, contrary to simple models, which generally predict high anisotropy of electrons and X-rays, it was found that the observed hard X-ray directivities are low (e.g. Kane 1983). Furthermore, Kontar & Brown (2006) found a low anisotropy of the electron distribution function in the X-ray source by separating the reflected X-ray emission from the direct one. They concluded that the conventional solar flare models with downward beaming are excluded.

In the present paper we want to demonstrate the importance of the abovementioned processes on the evolution of the beam-plasma system with the return current. Our aim is to show their effects on the anisotropy of the electron distribution function in this system and thus on the directivity of the corresponding X-ray emission. Using the 3-D electromagnetic PIC model, for the first time in the study of X-ray directivity, we compute the evolution of the beam-plasma system with the return current depending on the magnetic field in the beam propagation direction. Then, assuming that the resulting electron distribution functions generate X-ray bremsstrahlung, we calculate the directivity of the associated X-ray emission. (For a detailed analysis of the instabilities and waves produced in the studied beam-plasma system, see Karlický et al. 2008; Karlický 2009; Karlický & Bárta 2009.)

The layout of the paper is as follows: in Sect. 2 we outline our model. The results of computations of the electron

Table 1. Model parameters.

Model	m_i/m_e	n_b/n_e	v_b/c	ω_{ce}/ω_{pe}
A	16	1/8	0.666	0.0
B	16	1/8	0.666	0.1
C	16	1/8	0.666	0.5
D	16	1/8	0.666	0.7
E	16	1/8	0.666	1.0
F	16	1/8	0.666	1.3
G	1	1/8	0.666	0.0
H	1	1/8	0.666	1.3
I	100	1/8	0.666	0.0
J	100	1/8	0.666	1.3
K	16	1/8	0.333	0.0
L	16	1/8	0.333	1.3
M	16	1/40	0.666	0.0
N	16	1/8	0.234[a]	0.0
O	16	1/8	0.234[b]	1.3

[a] Mean velocity of the power-law beam distribution; [b] mean velocity of the power-law beam distribution.

distribution functions with the return current are shown in Sect. 3. In Sect. 4 we present the corresponding X-ray directivities. Finally, in Section 5 the results are discussed and conclusions given.

2. Model

For our study we used a 3-D (3 spatial and 3 velocity components) relativistic electromagnetic PIC code (Buneman 1993). The system sizes are $L_x = 45\Delta$, $L_y = 45\Delta$, and $L_z = 600\Delta$ (where Δ is the grid size).

For a basic set of models we initiated a spatially homogeneous electron-proton plasma with the proton-electron mass ratio $m_p/m_e = 16$ (Models A-F, and K-O in Table 1). This is unrealistic and it was chosen to shorten the proton skin depth and computations. Nevertheless, the ratio is still sufficient to well separate the dynamics of electrons and protons. For comparison we added models with the mass ratio $m_p/m_e = 1$ and 100 (Models G-J in Table 1). The electron thermal velocity is $v_{Te} = 0.06\,c$ (the corresponding temperature is $T_e = 21.4$ MK), where c is the speed of light. In all models, 160 electrons and 160 protons per cube grid were used. The plasma frequency is $\omega_{pe} = 0.05$ and the electron Debye length is $\lambda_D = 0.6\,\Delta$. In the models with the proton-electron mass ratio $m_p/m_e = 16$, the electron and proton skin depths are $\lambda_{ce} = 10\Delta$ and $\lambda_{ci} = 40\Delta$, respectively.

Then, we included one monoenergetic beam homogeneous throughout the numerical box (see Models A-M). Note that due to the physical and numerical simplicity and the propagation effect in which faster electrons escape from the slower ones, in most cases we consider monoenergetic electron beams, although in the interpretation of solar flare hard X-rays, the power-law distributions are used. The power-law distributions are derived as mean distributions over the whole X-ray source for much longer timescales than those considered in the present study. In much smaller flare volumes and on much shorter timescales, the monoenergetic beam is a reasonable choice. Nevertheless, in Models N and O we added computations with the beam having a power-law distribution function. To show effects of instabilities distinctly we chose its power-law index (in the velocity space) as 1.5, and the low-velocity cutoff of 0.09 c.

To keep the total current zero in these models in the initial states, we shifted the background plasma electrons in the velocity space (i.e. we initiated the return current) according to the relation $v_d = -v_b n_b/n_e$, where v_b is the velocity of the electron beam, n_b and n_e are the beam and background plasma densities (for this type of initiation see Niemiec et al. 2008). The beam velocity was chosen to be $v_b/c = 0.666$ or 0.333 (in the z direction), see Table 1. The ratio of the beam and plasma densities was taken as $n_b/n_e = 1/8$ (Models A-L and N-O), and $n_b/n_e = 1/40$ (Model M).

Because computations in the PIC models are dimensionless, the results are valid for a broad range of plasma densities. The real time and spatial scales are given by specifying the plasma density. Table 2 summarizes temporal and spatial scales (the interval of computations $t = 200/\omega_{pe}$ and the Debye length) for the plasma densities in the 10^8–10^{11} cm^{-3} range. The processes under study are very fast. The collisional processes are much longer, see the collisional free time ($1/\nu_0$) in Table 2. The numerical system size is small ($45\Delta \times 45\,\Delta \times 600\,\Delta = 75\lambda_D \times 75\lambda_D \times 1000\lambda_D$, i.e. for the plasma density e.g. $n_e = 10^9$ cm^{-3} it gives 76 cm × 76 cm × 1010 cm). Since the periodic boundary conditions are used, in reality the studied problem is infinite in space.

The beam density and the corresponding beam energy flux is given by the chosen plasma density n_e, $n_b/n_e = (1/8$ and $1/40)$, and the beam velocities (see Table 1). For example, for $n_e = 10^9$ cm^{-3}, $n_b/n_e = 1/8$, and $v_b = 0.666\,c$, the beam density $n_b = 1.25 \times 10^8$ cm^{-3} and the beam energy flux $E_{flux} = 4.55 \times 10^{11}$ erg s^{-1} cm^{-3}.

Table 2. The real spatial and time scales as a function of the chosen plasma density n_e.

n_e (cm^{-3})	ω_{pe} (s^{-1})	$t = 200/\omega_{pe}$ (s)	λ_D (cm)	$1/\nu_0$ (s)
10^8	5.64×10^8	3.55×10^{-7}	3.19	3.61
10^9	1.78×10^9	1.12×10^{-7}	1.01	0.36
10^{10}	5.64×10^9	3.55×10^{-8}	0.32	0.03
10^{11}	1.78×10^{10}	1.12×10^{-8}	0.10	0.003

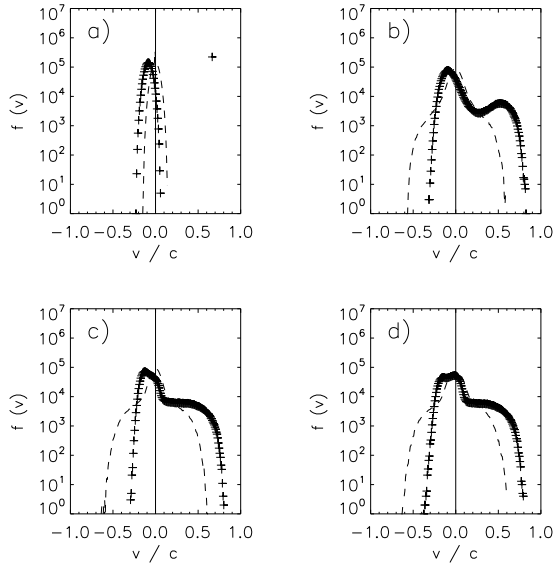

Fig. 1. The electron distribution functions in Model B at four different times: at the initial state **a)**, at $\omega_{pe}t = 40$ **b)**, at $\omega_{pe}t = 100$ **c)**, and $\omega_{pe}t = 200$ **d)**. Crosses correspond to $f(v_z)$, dotted and dashed lines display $f(v_x)$ and $f(v_y)$, respectively. Note that $f(v_x)$ and $f(v_y)$ overlap. The single cross in the part **a)** at $v/c = 0.666$ denotes the monoenergetic electron beam.

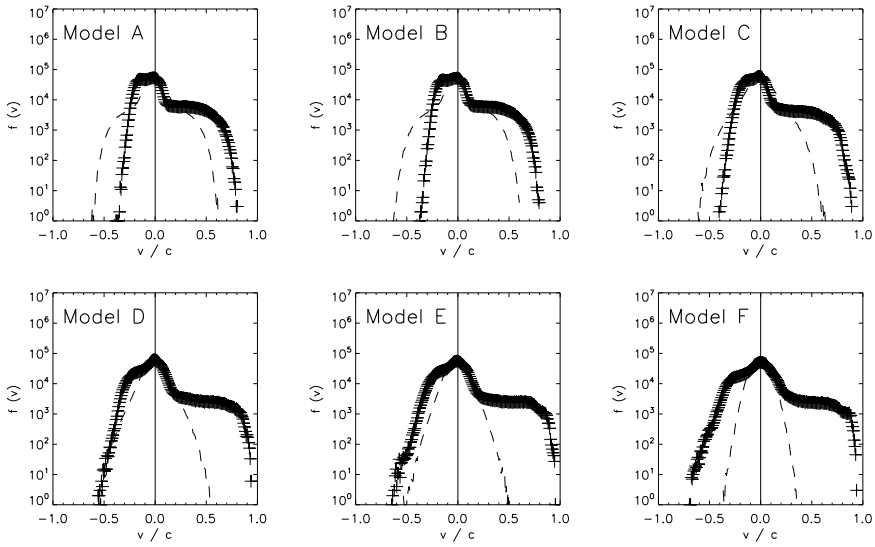

Fig. 2. The electron distribution functions at $\omega_{pe}t = 200$ as a function of the magnetic field in Models A-F with $\omega_{ce}/\omega_{pe} = 0.0$, 0.1, 0.5, 0.7, 1.0, and 1.3, respectively. Notation is the same as in Fig. 1.

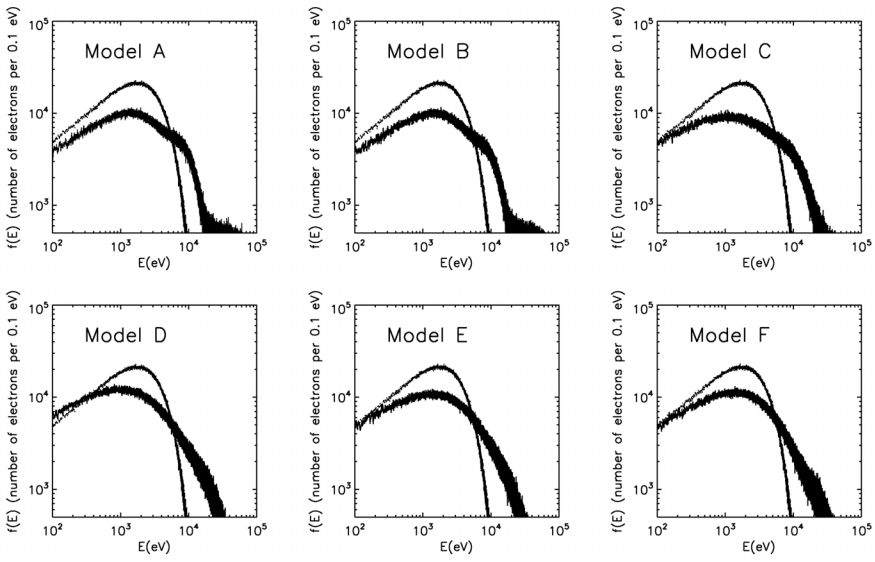

Fig. 3. The electron distribution functions in electron energies (thick lines) at $\omega_{pe}t = 200$ as a function of the magnetic field in Models A-F with $\omega_{ce}/\omega_{pe} = 0.0$, 0.1, 0.5, 0.7, 1.0, and 1.3, respectively. For comparison in each panel the initial electron plasma distribution is added (thinner lines).

Because we want to study the influence of the magnetic field, in the models we consider several values of the ratio of the electron-cyclotron and electron-plasma frequencies ($\omega_{ce}/\omega_{pe} = 0.0$, 0.1, 0.5, 0.7, 1.0, and 1.3 – see Table 1). Note that in the space close to the flare acceleration site in the low corona there is plasma of relatively low density. Thus, for the huge electron beam fluxes required for an explanation of the observed X-ray bursts, such high ratios of n_b/n_e are needed. In all models, the periodic boundary conditions were used.

3. Results of 3-D PIC simulations

As an illustration of the time evolution of the electron distribution function in the beam-plasma system with the return current, Fig. 1 shows this evolution for Model B. As can be seen, due to the two-stream instability (Michailovskij 1975), a plateau of the distribution function $f(v_z)$ (in the beam propagation direction) on the beam side is formed. Moreover, some small part of the electrons even increased their energy due to their interaction with generated Langmuir waves. Simultaneously, the distribution functions $f(v_x)$ and $f(v_y)$, i.e. the distribution functions in the directions perpendicular to that of the beam propagation, are strongly heated. This is due to the Weibel instability (1959, see also Nishikawa et al. 2006).

To demonstrate how the magnetic field influences the resulting electron distribution function, Fig. 2 presents the distribution functions for six values of the ratio of the electron-cyclotron and electron-plasma frequencies ($\omega_{ce}/\omega_{pe} = 0.0$, 0.1,0.5, 0.7, 1.0, and 1.3 – Models A-F, Table 1). It is evident that with the increase of the ratio ω_{ce}/ω_{pe}, the role of the Weibel instability is more and more reduced, the distribution functions in the direction perpendicular to the beam propagation $f(v_x)$ and $f(v_y)$ are less heated. On the other hand, the problem of the return current formation becomes more and more one-dimensional and a more extended tail on the return current side is formed (compare Model A and F in Fig. 2, see also Karlický et al. 2008; Karlický 2009; Karlický & Bárta 2009). In Fig. 3 the same results are expressed in terms of the electron distribution functions depending on the electron energies. Although this type of description is more common in flare research, the distribution functions in velocity space presented in Fig. 2 carry more information than those in Fig. 3 and thus they are more physically relevant in describing the studied processes. The ratio of the electron kinetic energies in the direction parallel and perpendicular to that

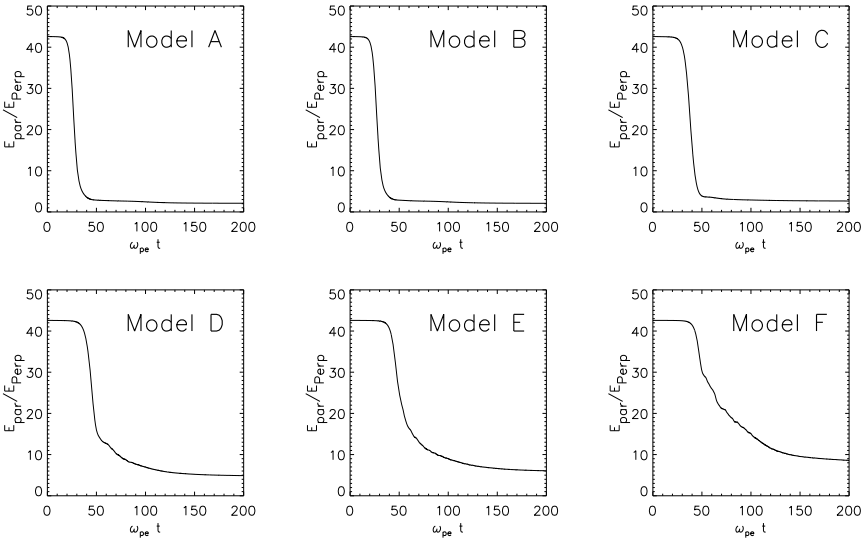

Fig. 4. Time evolution of the ratio of the electron kinetic parallel and perpendicular energies $E_{\rm par}/E_{\rm per}$ as a function of the magnetic field in Models A-F with $\omega_{\rm ce}/\omega_{\rm pe}$ = 0.0, 0.1, 0.5, 0.7, 1.0, and 1.3, respectively.

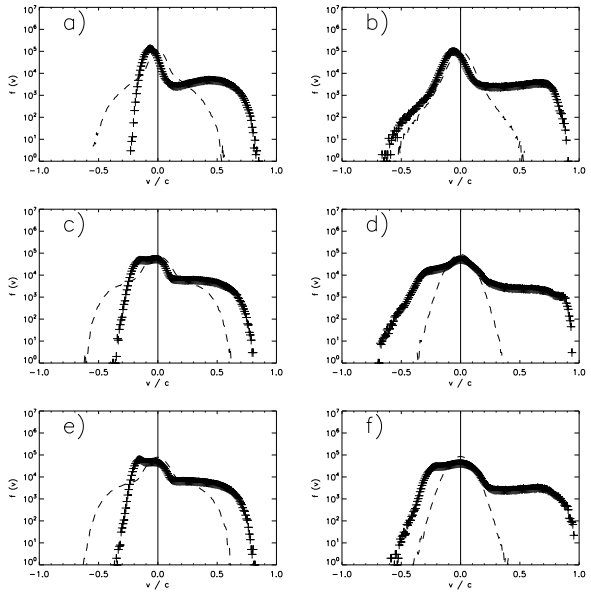

Fig. 5. The electron distribution functions at $\omega_{\rm pe}t$ = 200 as a function of the mass ratio: $m_{\rm i}/m_{\rm e}$ = 1 – two upper plots, $m_{\rm i}/m_{\rm e}$ = 16 – two middle plots, and $m_{\rm i}/m_{\rm e}$ = 100 – two bottom plots for two values of $\omega_{\rm ce}/\omega_{\rm pe}$ = 0.0 (*left column*) and 1.3 (*right column*). Notation is the same as in Fig. 1.

of beam propagation, which expresses the "anisotropy" of the system, is shown in Fig. 4. The ratio of energies is defined as:

$$\frac{E_{\rm par}}{E_{\rm perp}} = \frac{\sum_{i=1}^{n} \frac{1}{2} m_{\rm e} v_{iz}^2}{\sum_{i=1}^{n} \frac{1}{4} m_{\rm e} (v_{ix}^2 + v_{iy}^2)}, \quad (1)$$

where n is the number of electrons in the whole numerical box. As can be seen in Fig. 4, the collisionless (wave-particle) processes very rapidly decrease the "anisotropy" on time scales shorter than $\omega_{\rm pe}t \approx 50$. This process is faster and more efficient for lower magnetic fields. While the ending ratio is $E_{\rm par}/E_{\rm perp} \approx 9$ for Model F ($\omega_{\rm ce}/\omega_{\rm pe}$ = 1.3), in Model A ($\omega_{\rm ce}/\omega_{\rm pe}$ = 0.0) this ratio is only $E_{\rm par}/E_{\rm perp} \approx 2$.

In Fig. 5 a comparison of models with three different mass ratios ($m_{\rm p}/m_{\rm e}$ = 1, 16, 100) and two values of the ratio $\omega_{\rm ce}/\omega_{\rm pe}$ (0.0 and 1.3) is made. While in the cases with $m_{\rm p}/m_{\rm e}$ = 1 (the electron-positron plasma) the strong heating of the distribution functions $f(v_x)$ and $f(v_y)$ can be seen even for the strong magnetic field ($\omega_{\rm ce}/\omega_{\rm pe}$ = 1.3), for the proton-electron plasma the resulting $f(v_x)$ and $f(v_y)$ for $m_{\rm p}/m_{\rm e}$ = 16 and 100 do not differ significantly. Note that in the model with $m_{\rm p}/m_{\rm e}$ = 100 the proton skin depth is greater than the system sizes L_x and L_y.

We also compared the evolution of the electron distribution functions in Models A and F with Models K and L, i.e. the models with a lower initial beam velocity ($v_{\rm b}/c$ = 0.333). We found that only the extent of the return-current tail in Model L is shorter than that in Model F. It is a natural consequence of the greater beam velocity in Model F than in Model L. Furthermore, it was found that Model M gave qualitatively the same results as Model A.

In Figs. 6 and 7 the electron distribution functions in Models N and O, i.e. in the models with the power-law beam and with two different ratio of electron-cyclotron and electron-plasma frequencies ($\omega_{\rm ce}/\omega_{\rm pe}$ = 0.0 and 1.3) are shown. Because these models are not subject to the bump-on-tail instability there are no significant changes in the distribution $f(v_z)$ on the beam distribution side. On the other hand, the Weibel instability plays its role, especially in the case without the magnetic field (Model N). Once again, in Model N the plasma is heated in the direction perpendicular to that of beam propagation, whereas in Model O, the return current is formed by the extended distribution tail.

4. Directivity of X-ray emission

Knowing the electron distribution function $f(\boldsymbol{v})$, an instantaneous X-ray bremsstrahlung, i.e. the so-called thin-target emission (e.g. Brown et al. 2003) can be calculated. To account for the anisotropy of $f(\boldsymbol{v})$, we considered the angle-dependent electron-ion bremsstrahlung cross-section $Q(\epsilon, E, \Theta)$ differential in the electron energy E and the solid angle of the incoming electron, where ϵ is the photon energy and Θ is the angle between the electron pre-collision velocity and direction of the photon emission (Gluckstern & Hull 1953). We used the expression for $Q(\epsilon, E, \theta)$ given in Appendix of Massone et al. (2004), which includes the Elwert (1939) Coulomb correction. The cross-section was evaluated using `hsi_reg_ge_angle_cross.pro` available in the Solar Software.

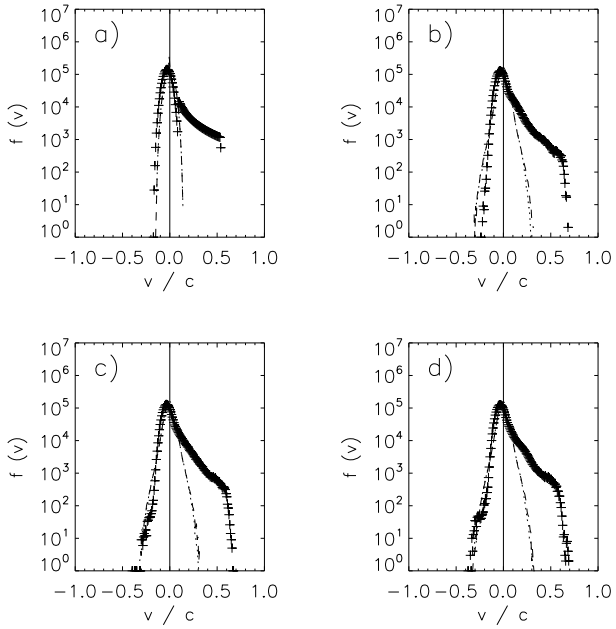

Fig. 6. The electron distribution functions in Model N with the power-law beam at four different times: at the initial state **a)**, at $\omega_{pe}t = 40$ **b)**, at $\omega_{pe}t = 100$ **c)**, and $\omega_{pe}t = 200$ **d)**. Notation is the same as in Fig. 1.

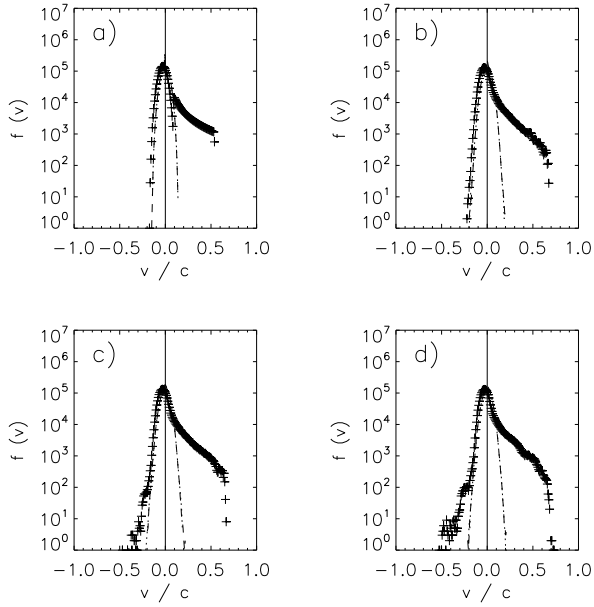

Fig. 7. The electron distribution functions in Model O with the power-law beam at four different times: at the initial state **a)**, at $\omega_{pe}t = 40$ **b)**, at $\omega_{pe}t = 100$ **c)**, and $\omega_{pe}t = 200$ **d)**. Notation is the same as in Fig. 1.

Figure 8 shows the X-ray directivity, i.e. the ratio of the angle-dependent $I(\epsilon, \theta)$ to integral photon spectrum $I(\epsilon) = 1/4\pi \int_\Omega I(\epsilon, \theta, \phi)\, \mathrm{d}\Omega$, where θ and ϕ is the polar and azimuthal angle, respectively, Ω is the solid angle. The z-axis of the coordinate system is chosen to be along the beam propagation direction. Note that due to axial symmetry of the problem around the z-axis, the photon spectrum $I(\epsilon, \theta, \phi)$ is also independent of ϕ, so $I(\epsilon, \theta) = I(\epsilon, \theta, \phi)$. Assuming that the beam propagates along the local normal line towards the photosphere, Fig. 8 displays a variation of the X-ray directivity observed from different viewing angles: the cases with $\cos\theta = 1$ and $\cos\theta = -1$ correspond to the forward (the direction to the photosphere) and backward (the direction to the Earth's observer when the X-ray source is at the disc centre) emissions, while the case with $\cos\theta = 0$ denotes the emission in the perpendicular direction (the X-ray source placed on the solar limb).

The behaviour of the X-ray directivity is closely related to the corresponding electron distribution. Comparing Model A and F at the time $\omega_{pe}t = 200$ with Models A-F in the initial state (i.e. the case with a simple beaming) in Fig. 8, it can be seen that values of the directivity, especially in the backward direction, become closer to the value 1 (the isotropic case). Therefore, the global directivity decreased during the evolution of the electron distribution. Furthermore, we can see that the directivity values for $\cos\theta = 0$ in Model A are closer to the isotropic case than those in Model F. This is due to the strong heating of the plasma in the direction perpendicular to the beam propagation and it is caused by the Weibel instability in Model A (the case with zero magnetic field).

We also defined the electron directivity $f(E, \theta)/f(E)$, similarly to the X-ray one. Models A and F at time $\omega_{pe}t = 200$ are presented in Fig. 9 and show in another way the electron distribution characteristics discussed above in Sect. 3, Fig. 2. Comparing these electron directivities, we can see that they differ more distinctly than the corresponding X-ray directivities (Fig. 8). Such a difference is caused by the strong smoothing effect of the bremsstrahlung cross-section.

We also calculated the X-ray directivities for Models K-L and N-O. They show the same changes as follows from the comparison of plots in Fig. 8, but these changes are less pronounced due to smaller changes of the $f(\boldsymbol{v})$ anisotropy in these models.

5. Discussion and conclusions

Varying the ratio of electron-cyclotron and electron-plasma frequencies ω_{ce}/ω_{pe}, it was found that the magnetic field influences the evolution of the electron distribution function in electron beam – plasma system with a return current. While for small magnetic fields ($\omega_{ce}/\omega_{pe} \leq 0.1$) the electron distribution function becomes broad in the direction perpendicular to the beam propagation due to the Weibel instability and the return current is formed by the electrons in a broad and shifted bulk of the distribution, for stronger magnetic fields ($\omega_{ce}/\omega_{pe} \geq 1$) the distribution is more extended in the beam-propagation direction and the return current is formed by the electrons in an extended distribution tail. Assuming the magnetic field and electron density as $B = 100$ G and $n_e = 10^{11}$ cm^{-3} relevant to solar flares, the ratio of the electron-cyclotron and electron-plasma frequencies is $\omega_{ce}/\omega_{pe} = 0.1$. In such conditions the Weibel instability plays a role, but it is reduced for a higher magnetic field. The evolution is influenced also by the two-stream instability. Besides the formation of the plateau of the electron distribution on the electron beam side, the simultaneously generated Langmuir waves even accelerate a small part of the electrons.

The collisionless processes cause a very fast decrease of the ratio of the electron kinetic parallel and perpendicular (with respect to the beam propagation direction) energies and lead to a decrease of the "anisotropy" of the system. Thus, the distribution function rapidly deviates from that with simple beaming. This can be also expressed by a decrease of the directivity of the associated X-ray bremsstrahlung emission. This fact agrees with the statement of Kontar & Brown (2006) that conventional solar flare models with a simple downward beaming should be excluded.

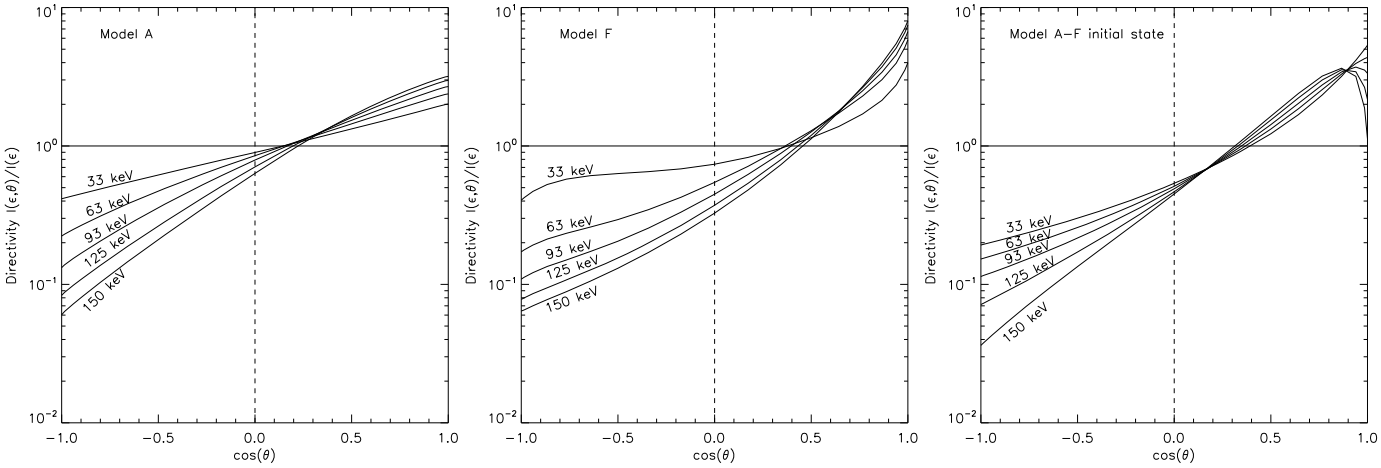

Fig. 8. The X-ray directivity in several energies for $f(\boldsymbol{v})$ corresponding to Models A and F at $\omega_{pe}t = 200$ and the X-ray directivity in the initial state for Models A-F (the case of simple beaming). The horizontal solid line represents the isotropic case, the dashed vertical line denotes the viewing angle for a limb source.

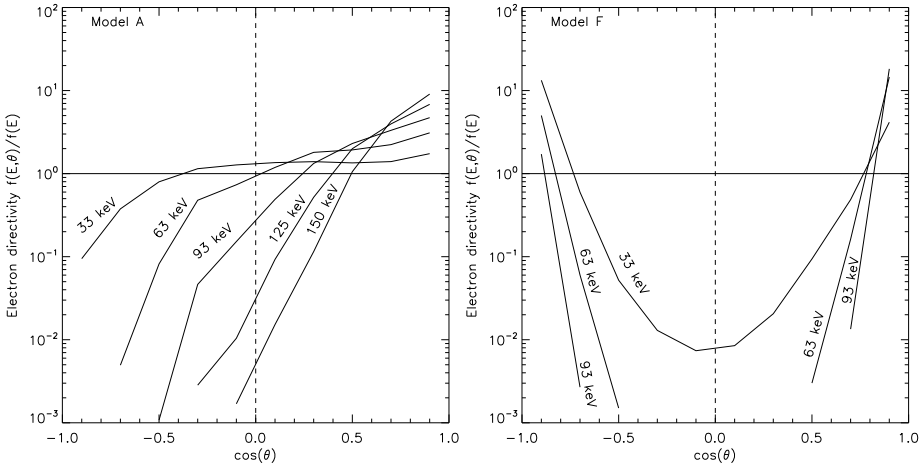

Fig. 9. The electron directivity in several energies for Models A and F at $\omega_{pe}t = 200$. The horizontal solid line represents the isotropic case, the dashed vertical line denotes the viewing angle for a limb source. The corresponding X-ray directivities are shown in Fig. 8.

An additional aspect of the present study is that the inclusion and physical necessity of the return current in the beam – plasma system resolves the problem of number of electrons needed for an acceleration of the dense electron beam in the corona where the density is relatively low. The return current simply carries the same amount of electrons as in the electron beam back to the acceleration site. However, the return current does not have the same distribution function as the initially injected beam.

Variations of the X-ray directivity obtained in our models are of a level comparable to those in the electron beam propagation models by Langer & Petrosian (1977, Fig. 1) and Leach & Petrosian (1983, Fig. 4). However, there is an important difference between our model and the models by Langer & Petrosian (1977) and Leach & Petrosian (1983). We treat only collisionless processes which were neglected in the previous studies. Due to the very short time scales in our computations, no effects of longer beam propagation or collision scattering are included in the electron beam evolution.

Therefore, the similar level of X-ray directivies suggests that a comparable level of isotropisation of the electron distribution function caused by the collisional processes can be produced by the studied wave-particle processes on much shorter time scales. Moreover, it means that these fast processes should not be neglected in X-ray directivity studies.

Our study is not aimed at a direct comparison with observations, mainly due to the large difference between simulated and observationally available time scales. Nevertheless, the paper by Kontar & Brown (2006) allows us to compare our simulations with their derived ratio of downward-to-upward electron distributions, $F_d(E)/F_u(E)$. The comparison reveals an agreement between inferred $F_d(E)/F_u(E)$ and Model F within the confidence interval up to ~50 keV. At higher energies, our models predict a directivity higher than that obtained from observations.

The results presented here could be appropriate for low-density parts of flare loops where the collisionless processes are dominant. Furthermore, one may consider them as input into simulations (on much longer time scales) which treat a propagation of the beam in the environment where Coulomb collisions play a significant role, such as the transition region and the chromosphere. Since all these processes (collisionless on long time scales, collisional and even ionization processes in the background plasma) lead to further isotropisation of the particle distribution, we speculate that the resulting electron distribution and X-ray directivity would be much closer to the isotropic case, as was recently found from X-ray observations (Kontar & Brown 2006).

Acknowledgements. All computations were performed on the parallel computer OCAS (Ondřejov Cluster for Astrophysical Simulations, see http://wave.asu.cas.cz/ocas). This research was supported by the grant IAA300030701 (GA ČR) and the research project AV0Z10030501 (Astronomical Institute). The authors thank the referee for constructive comments that improved the paper.

References

Benz, A. O. 1993, Plasma Astrophysics (Dordrecht, The Netherland: Kluwer Acad. Publ.)
Birdsall, Ch. K., & Langdon, A. B. 1985, Plasma Physics via computer simulation (USA: McGraw-Hill Book Comp.)
Bohm, D., & Gross, E. P. 1949, Phys. Rev., 75, 1851
Bret, A. 2009, ApJ, 699, 990
Brown, J. C. 1971, Sol. Phys., 18, 489
Brown, J. C., Karlický, M., MacKinnon, A. L., & van den Oord, G. H. J. 1990, ApJS, 73, 343
Brown, J. C., Emslie, A. G., & Kontar, E. P. 2003, ApJ, 595, L115
Buneman, O. 1993, in Computer Space Plasma Physics, ed. H. Matsumoto, & Y. Omura (Tokyo: Terra Scientific Publ. Comp.), 305
Elwert, G. 1939, Ann. Phys., 34, 178
Gluckstern, R. L., & Hull, M. H. 1953, Ohys. Rev., 90, 1030
Hoyng, P., Knight, J. W., & Spicer, D. S. 1978, Sol. Phys., 58, 139
Kane, S. R. 1983, Sol. Phys., 86, 355
Karlický, M. 1997, Space Sci. Rev., 81, 143
Karlický, M. 2009, ApJ, 690, 189
Karlický, M., & Bárta, M. 2009, Nonlinear Processes in Geophysics, 16, 525
Karlický, M., Nickeler, D. H., & Bárta, M. 2008, A&A, 486, 325
Kontar, E. P., & Brown, J. C. 2006, ApJ, 653, L149
Langer, S. H., & Petrosian, V. 1977, ApJ, 215, 666
Leach, J., & Petrosian, V. 1983, ApJ, 269, 715
Massone, A. M., Emslie, A. G., Kontar, E. P., et al. 2004, ApJ, 612, 1233
Melrose, D. B. 1980, Plasma Astrophysics (New York, USA: Gordon and Breach Sci. Publ.)
Michailovskij, A. B. 1975, Teorija plazmennych neustojchivostej, Atomizdat, Moskva (in Russian)
Niemiec, J., Pohl, M., Stroman, T., & Nishikawa, K. 2008, ApJ, 684, 1174
Nishikawa, K.-I., Hardee, P. E., Hededal, C. B., & Fishman, G. J. 2006, ApJ, 642, 1267
Tandberg-Hanssen, E., & Emslie, A. G. 1988, The Physics of Solar Flares (Cambridge, UK: Cambridge Univ. Press)
van den Oord, G. H. 1990, A&A, 234, 496
Weibel, E. S. 1959, Phys. Rev. Lett., 2, 83